

Morphology-engineered nanostructured silver- and antimony-telluride films for flexible thermoelectric generators

Ankit Kashyap^{a,b}, Conner Wallace^b, Geetu Sharma^b, Collin Rowe^b, Mahima Sasikumar^b, Niraj Kumar Singh^d, Per Eklund^{d,e}, Theodorian Borca-Tasciuc^c, Ganpati Ramanath^{b,d,e*}, and Ajay Soni^{a*}

^a*School of Physical Sciences, Indian Institute of Technology Mandi, 175005, Himachal Pradesh, India.*

^b*Rensselaer Polytechnic Institute, Materials Science & Engineering Department, Troy, NY 12180, USA.*

^c*Rensselaer Polytechnic Institute, Department of Mechanical Engineering, Troy, NY 12180, USA.*

^d*Inorganic Chemistry, Ångström Laboratory, Uppsala University, SE-751 21 Uppsala, Sweden.*

^e*Wallenberg Initiative Materials Science for Sustainability (WISE), Uppsala University, Sweden.*

*Corresponding authors: ganapr@rpi.edu, ganpati.ramanath@kemi.uu.se and ajay@iitmandi.ac.in

Abstract

Harvesting low-grade heat to electricity is attractive for powering wearable electronic devices. Here, we demonstrate nW-scale thermoelectric power generation in devices from thin film assemblies of microwave-synthesized p-Sb₂Te₃ nanoplates and n-Ag₂Te nanowires on polyvinylidene fluoride (PVDF) membranes. While microwave cycling is crucial for Ag₂Te nanocrystal shaping, Sb₂Te₃ formation is sensitive to precursors and surfactant concentrations. Introducing S doping in Sb₂Te₃ in the 1 ≤ x_S ≤ 1.5 at.% range via thioglycolic acid during synthesis yields an up to eightfold higher power-factor, due to a fivefold increase in electrical conductivity and ~25% increase in Seebeck coefficient. Our microfilm devices generate up to 33.6 mV from 5 °C ≤ ΔT ≤ 50 °C thermal gradients, with ~120 nW maximum power output at ΔT = 30 °C, which is sixtyfold higher than Sb₂Te₃ paper devices. Mechanical bending can increase device resistance by up to ~125% due to diminished inter-nanostructure electronic transport. These findings provide insights for integrating synthesis, morphology engineering and device design for next-generation wearable thermoelectric systems.

Keywords: Microwave synthesis, nanoplates, nanowires, flexible thermoelectric devices

1. Introduction

Wearable electronic devices for diverse applications¹ in physiological monitoring², sensing³, and diagnostics, are typically powered by micro-/milli-watt batteries. Solid-state thermoelectric power generators on flexible substrates^{2, 4,5} are attractive alternatives that eliminate recharging, replacement, and electrolyte leakage⁶ issues in batteries. Efficient thermoelectric generators require materials with high figure-of-merit⁷ $ZT = \frac{\alpha^2 \sigma T}{\kappa}$, which in turn requires a high Seebeck coefficient α , high electric

conductivity σ , low thermal conductivity κ at operating temperature T , along with well-engineered p-n junctions and metal/thermoelectric interfaces⁸⁻¹².

Integrating high ZT inorganic thermoelectrics¹³ with organic substrates is attractive for mechanically flexible high-efficiency thermoelectric power generators¹⁴. For instance, the high ZT of pnictogen chalcogenides¹⁵⁻¹⁷ can be increased further by nanostructuring-induced decrease in κ , and maximizing power factor $\alpha^2\sigma$ via doping and alloying^{17, 18} to manipulate the electronic structure. However, integrating these inherently inorganic brittle materials with organic substrates is a challenging task¹⁹⁻²². One strategy to circumvent cracking is to use thin film assemblies of inorganic nanostructures, which offer enhanced mechanical compliance and improved structural stability²³.

Thin film assemblies of n-type Ag_2Te ^{14, 24} and p-type Sb_2Te_3 ^{15, 16} nanostructures exhibit high $\alpha^2\sigma$ near room temperature. Anisotropic 1-D and 2-D nanostructures often enhance ZT^{20, 25} through decreased thermal conductivity κ and high power factor from nanoscopic confinement effects. These findings have spurred studies of nanostructured thin films^{15, 26} of Ag_2Te and Sb_2Te_3 on flexible substrates (e.g., polyvinylidene fluoride –PVDF²⁰, nylon^{21, 27}, polyimide^{28, 29, 30}, paper³¹, and polytetrafluoroethylene²¹) by physical^{32, 33}/chemical³⁴ methods including vacuum filtration^{20, 27}, drop casting^{35, 36}, and inkjet/screen printing^{2, 37}. For instance, Ag_2Te /nylon devices²⁷ yield high power factors $\alpha^2\sigma \sim 513 \mu\text{W m}^{-1}\text{K}^2$ and $\sim 1.6 \mu\text{W}$ maximum power. Composites of Sb_2Te_3 /MXene³⁸ and Sb_2Te_3 /carbon nanotubes³⁹ and Bi_2Te_3 / Sb_2Te_3 films integrated with paper^{35, 36} yield ~ 40 - 45 mV at $\Delta T = 30$ - 50 °C, but the power output is low in the pW range.

Here, we demonstrate the performance of a thermoelectric power generator fabricated from microwave-synthesized Ag_2Te nanowires and sulfur-doped Sb_2Te_3 nanoplates on PVDF. The morphology engineering using microwave synthesis is ~ 50 - to 100-fold faster (e.g., ~ 10 minutes)^{15, 16, 18, 40} than solvothermal⁴¹⁻⁴³, polyol^{20, 44}, and electrodeposition methods⁴⁵ (e.g., ~ 24 hours)^{41, 43}. By varying the sulfur content in p- Sb_2Te_3 (1-1.5 at.%), we achieved significant improvements in carrier concentration and power factor $\alpha^2\sigma$. A six-leg thermoelectric device comprised of alternating strips of n- Ag_2Te and p- Sb_2Te_3 , generated ~ 33.6 mV at $\Delta T \sim 50$ °C and a power of ~ 120 nW at $\Delta T \sim 30$ °C. These results highlight a scalable approach to fabricate thermoelectric power generators for harvesting low-grade waste heat.

2. Experimental Section

2.1. Sb_2Te_3 nanoplate synthesis

Sb_2Te_3 nanoplates were synthesized by a microwave solvothermal process described elsewhere¹⁶. SbCl_3 , 95% pure thioglycolic acid (TGA), 95% pure 1,5-pentanediol, 99.8% pure 200-mesh Te powder, and tri-n-octylphosphine (TOP) obtained from Sigma Aldrich were used as-received. A homogeneous 0.15 mmol Te solution was obtained by dissolving Te powder in 2 ml TOP with 10 minutes sonication, followed by three cycles of ~ 900 W microwave exposure for ~ 1 - 2 minutes. The solution was then

cooled for ~1-2 minutes. In parallel, 225 ml TGA was added to a 0.30 mmol SbCl₃ solution in 6.25 ml 1,5-pentanediol and sonicated for ~20 minutes. This TGA-SbCl₃ solution was mixed with the Te solution and continuously stirred for ~5 minutes prior to a 2-minute microwave exposure. Cooling the reaction mixture to room temperature yielded dark grey precipitates which were centrifuged, repeatedly washed with acetone and isopropanol, and dried overnight at 60 °C.

2.2. Ag₂Te nanowire synthesis

Ag₂Te nanowires were synthesized by microwave-stimulation from as-received 97~98% pure NaOH and K₂TeO₃·H₂O, ~99.0% pure AgNO₃ and ethylene glycol, all from Sigma-Aldrich. First, a homogenous 4.95 mmol NaOH solution was prepared in 25 ml ethylene glycol by ultrasonication for ~ 60 minutes. In parallel, 0.5 mmol K₂TeO₃·H₂O was dissolved in ~15 ml ethylene glycol and ultrasonicated for ~ 30 minutes. Following this, ~1 mmol AgNO₃ was dissolved in ~ 5 ml ethylene glycol by continuous stirring for ~ 5 minutes, and mixed with the Te solution in an Erlenmeyer flask. The NaOH solution was added gradually to the Ag-Te solution mixture to obtain a black solution consisting of ~ 45 ml of 110 mM NaOH, 11 mM K₂TeO₃·H₂O, and 22 mM of AgNO₃.

This solution was exposed to repeated cycles of ~ 15-second microwave exposures followed by stirring. The first 10 microwave exposure cycles were separated by 10 seconds stirring intervals, the second 10 cycles were interspersed with 25 seconds stirring, and the last five cycles were spaced with 60 seconds stirring. The reaction temperature was maintained at 180–195 °C, with the sample exposed to an estimated ~ 270 kJ of microwave energy. The black precipitates obtained were separated by centrifugation, washed thoroughly with acetone and isopropanol, and dried overnight at 60 °C.

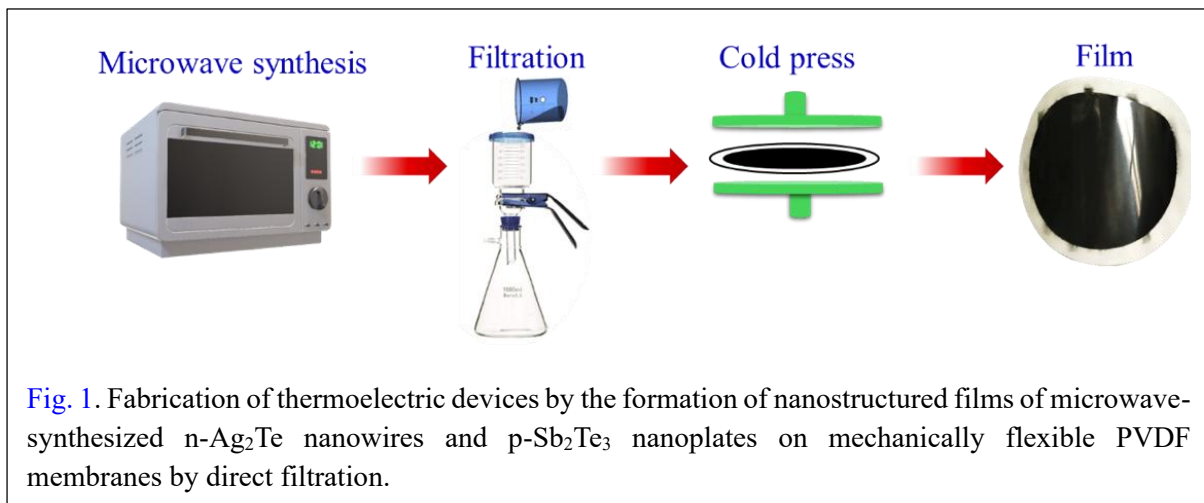
2.3. Device fabrication

Thin film assemblies of Sb₂Te₃ nanoplates and Ag₂Te nanowires were deposited on PVDF by vacuum filtration from 0.08 g powders of the respective materials dispersed in 20-ml ethanol solutions. These solutions were sonicated for ~10 minutes to ensure uniform nanoparticle dispersions. Vacuum filtration of the solution through a 47-mm PVDF membrane with 0.22 µm pores resulted in uniform films (Fig. 1) that were dried at 80 °C for ~10 minutes to remove solvent traces. The film was cold-pressed by gradually increasing the load from 0 to 7.5 metric tons. Alternate strips of 5 mm x 28 mm Sb₂Te₃/PVDF and Ag₂Te/PVDF structures were connected using Cu wires contacts capped with quick-dry Ag epoxy (SPI 04998-AB) applied using a needle to fabricate a 6-leg thermoelectric device.

2.4. Characterization and device performance testing

Output voltage and power characteristics were measured as a function of temperature gradient, ΔT, (Fig. S1a) applied using a hot plate and a water cooler aluminium block affixed with 100-µm-diameter E-type thermocouples. These measurements were carried out in a custom-built setup automated through a LabView interface to a Keithley source meter 2400 and a Keithley multimeter 2000 (Fig. S1b).

X-ray diffractograms (XRD) were obtained using a PANalytical instrument with a Cu K α probe beam for phase identification. A field-emission Zeiss Supra 55 SEM operated at 5-20 keV was used to characterize nanostructure morphology, flexible films thickness and determine chemical composition from energy-dispersive X-ray (EDX) spectra obtained at 20 keV. X-ray photoelectron spectroscopy (XPS) measurements in a PHI 5000 Versaprobe system were used to characterize the surface chemistry. XPS analyses used MultiPak software (ULVAC-PHI, Inc.) to subtract background by the Shirley method, and corrected charging-related energy shifts with reference to the adventitious carbon peak.⁴⁶ A second order Savitzky-Golay filter with a 10-point window was used to smoothen the oxidized S 2p spectra.



Electrical conductivity σ was determined with a Ossila T2001A four-point-probe station. The Seebeck coefficient α was determined from the Seebeck voltage measured with a Keithley 2001 multimeter⁴⁷ in a custom-built setup with the temperature gradient created by Peltier modules and measured by K-type thermocouples. Charge carrier concentration, n and mobility, μ were calculated from room-temperature Hall measurements in an apparatus with a ~ 0.485 T permanent magnet. Hall voltages were measured in van der Pauw geometry using a Keithley 2100 multimeter for a 10 mA current delivered by a Keithley 2400 source. The effect of mechanical deformation of the nanostructured films on PVDF on power output was tested by compressively flexing the film in an Instron 5843 system.

3. Results and discussion

3.1. Nanocrystal structure, morphology and composition

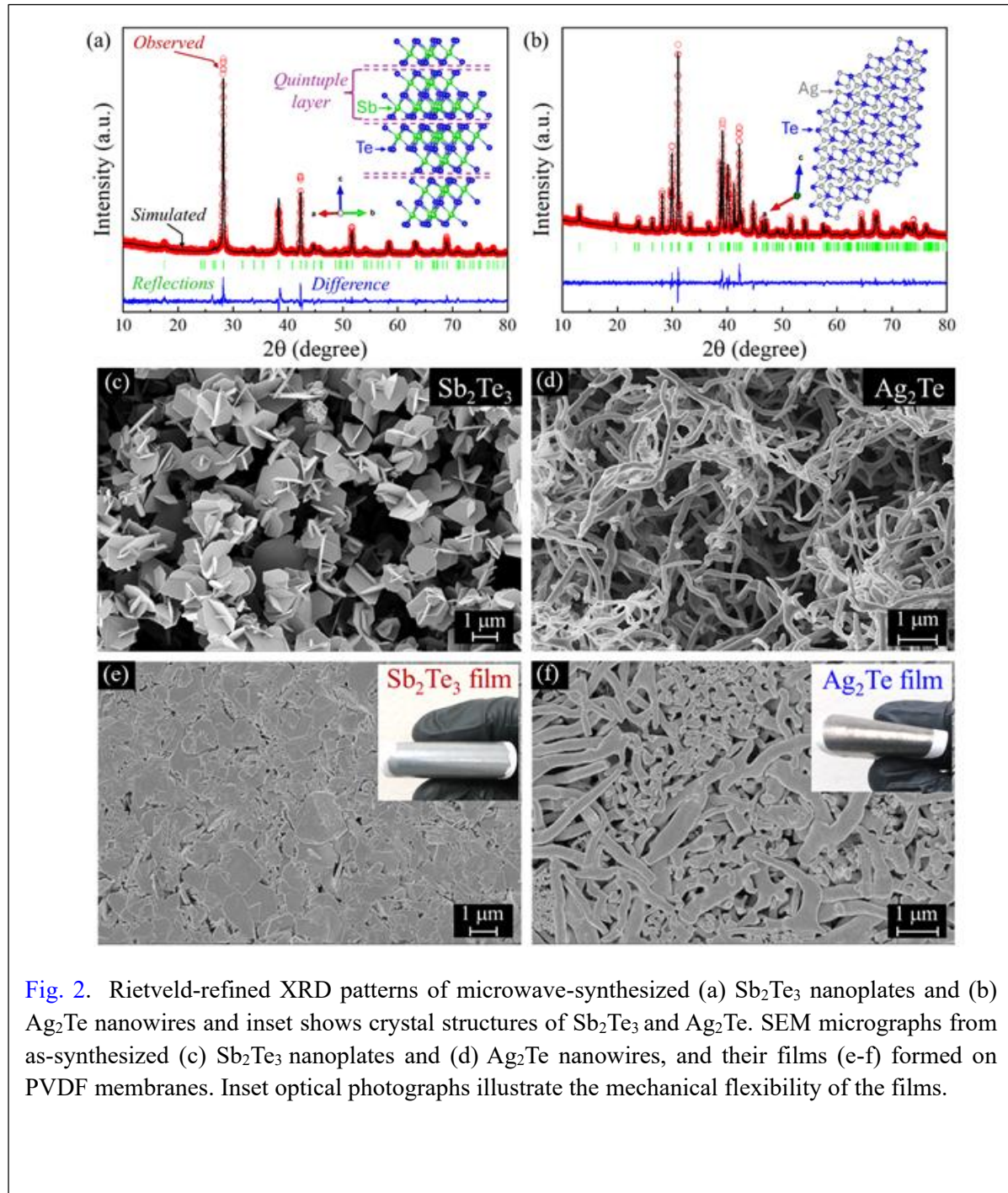
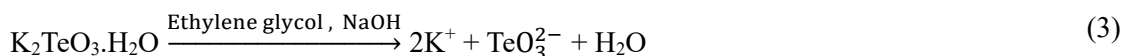


Fig. 2. Rietveld-refined XRD patterns of microwave-synthesized (a) Sb_2Te_3 nanoplates and (b) Ag_2Te nanowires and inset shows crystal structures of Sb_2Te_3 and Ag_2Te . SEM micrographs from as-synthesized (c) Sb_2Te_3 nanoplates and (d) Ag_2Te nanowires, and their films (e-f) formed on PVDF membranes. Inset optical photographs illustrate the mechanical flexibility of the films.

X-ray diffractograms show the presence of rhombohedral Sb_2Te_3 (JCPDS No. 15-874 with $\text{R}\bar{3}\text{m}$ space group), and monoclinic Ag_2Te (JCPDS No. 34-142, with $\text{P}2_1/\text{c}$ space group). The positions of the sharp peaks (Fig. 2a-b) from both materials agree with the JCPDS cards, indicating that microwave synthesis yields high quality and high purity materials. Unit cell dimensions obtained from Rietveld refinement analyses are listed in supplementary information Table S1. SEM images show hexagonal

Sb_2Te_3 nanoplates and branched Ag_2Te nanowires (Fig. 2c-d) with monomodal size distributions (see supplementary Fig. S2). EDX reveals uniform elemental distributions in Sb_2Te_3 and Ag_2Te nanostructures (see Fig. S3), highlighting compositional homogeneity. Ag_2Te nanostructure shape is sensitive to microwave cycling (Fig. S4). Pulsed microwave heating with on/off cycles yields Ag_2Te nanowires (Fig. S4a-b), in contrast to near-spherical Ag nanoparticles obtained by continuous heating (Fig. S4c-d). Microwave cycling likely provides sufficient time for TeO_3^{2-} reduction which is known to favor nanowire formation.⁴⁸

Ag_2Te nanostructures can be envisioned to form in five steps as follows. Ethylene glycol dehydration (1) yields acetaldehyde which reduces Ag^+ to produce Ag metal (2). Potassium tellurite ionization (3) yields TeO_3^{2-} ions which are reduced to Te metal (4), which combines with Ag to form Ag_2Te (5). The chemical reactions are as follows,



3.2. Effects of surfactants on phase formation and morphology

Microwave synthesis of Sb_2Te_3 is sensitive to precursors and surfactant concentrations (Figs. 3a-f), which provides significant scope to control Sb_2Te_3 nanostructure morphology and Te heterostructuring. The use of trioctylphosphine (TOP) surfactant yields Sb_2Te_3 (Figs. 3a-b). While 2 ml TOP yields well-formed hexagons, increasing TOP to 5 ml leads to the decoration of Te fins at platelet edges⁴⁰ (Figs. 3a-b). Replacing TOP with trioctylphosphine oxide (TOPO) produces Sb_2Te_3 with deformed hexagons morphology rough surface along with elemental Te (see Figs. S5a-b). Increasing the pentanediol content has a similar effect as increasing TOP; bare hexagon-shaped Sb_2Te_3 platelets give way Sb_2Te_3 -Te heterostructures with Te fins (Figs. 3c-d) reminiscent of prior works^{15, 40}. Low thioglycolic acid (TGA) concentrations (e.g., ~0.14 M) yield poorly-defined nanoplates due to non-uniform nucleation and growth (Fig. 3e). Hexagon-shaped Sb_2Te_3 nanoplates (Fig. 3f) are formed with 0.5 M TGA, in agreement with earlier studies⁴⁰. Besides shape control via selective passivation of Sb_2Te_3 crystal facets

by thiol moieties⁴⁹, TGA also facilitates sulfur doping¹⁵. Absolute precursor amounts also influence the Sb_2Te_3 morphology (Figs. S6a-b).

3.3. Partial oxidation

Core-level spectra from nanostructured Sb_2Te_3 and Ag_2Te films reveal surface oxidation (Figs. 4a-b; Fig. S8). The high binding energy Sb 3d_{3/2} and 3d_{5/2} peak components at ~ 538.2 eV and ~ 528.8 eV from Sb_2Te_3 films correspond to $\text{Sb}_2\text{Te}_x\text{O}_{3-x}$ (Fig. 4a). This is corroborated by the high-binding energy Te 3d_{5/2} – Te d_{3/2} components at ~ 576.4 eV and 586.7 eV, respectively indicating TeO_x (Fig. 4b). The

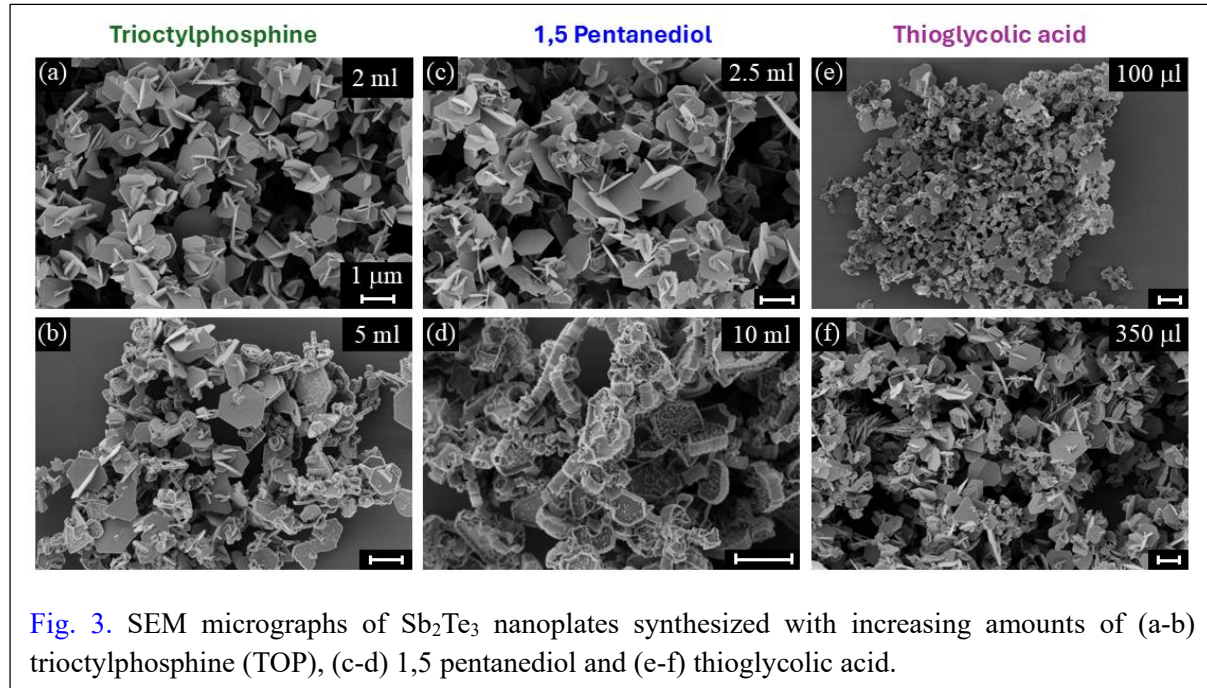


Fig. 3. SEM micrographs of Sb_2Te_3 nanoplates synthesized with increasing amounts of (a-b) trioctylphosphine (TOP), (c-d) 1,5 pentanediol and (e-f) thioglycolic acid.

presence of both unoxidized and oxidized Te components indicate partial surface oxidation. The 170 eV SO_x peak (Fig. 4b inset) confirms that the Sb_2Te_3 nanoplates are sulfur-doped. Thus TGA is a triple-agent for sulfur-doping and nanostructure-shaping¹⁶. Films of Ag_2Te nanowires show overlapping bands of Te 3d_{5/2} at ~ 572.8 eV and Ag 3p_{3/2} at ~ 573.2 eV (Fig. 4c-d), indicating partial surface oxidation with a nominal $\text{AgTe}_{0.1}\text{O}_{0.2}\text{C}_{0.4}$ stoichiometry. Fig. S9 shows TGA-induced increase in sulfur bands from Sb_2Te_3 films on PVDF film.

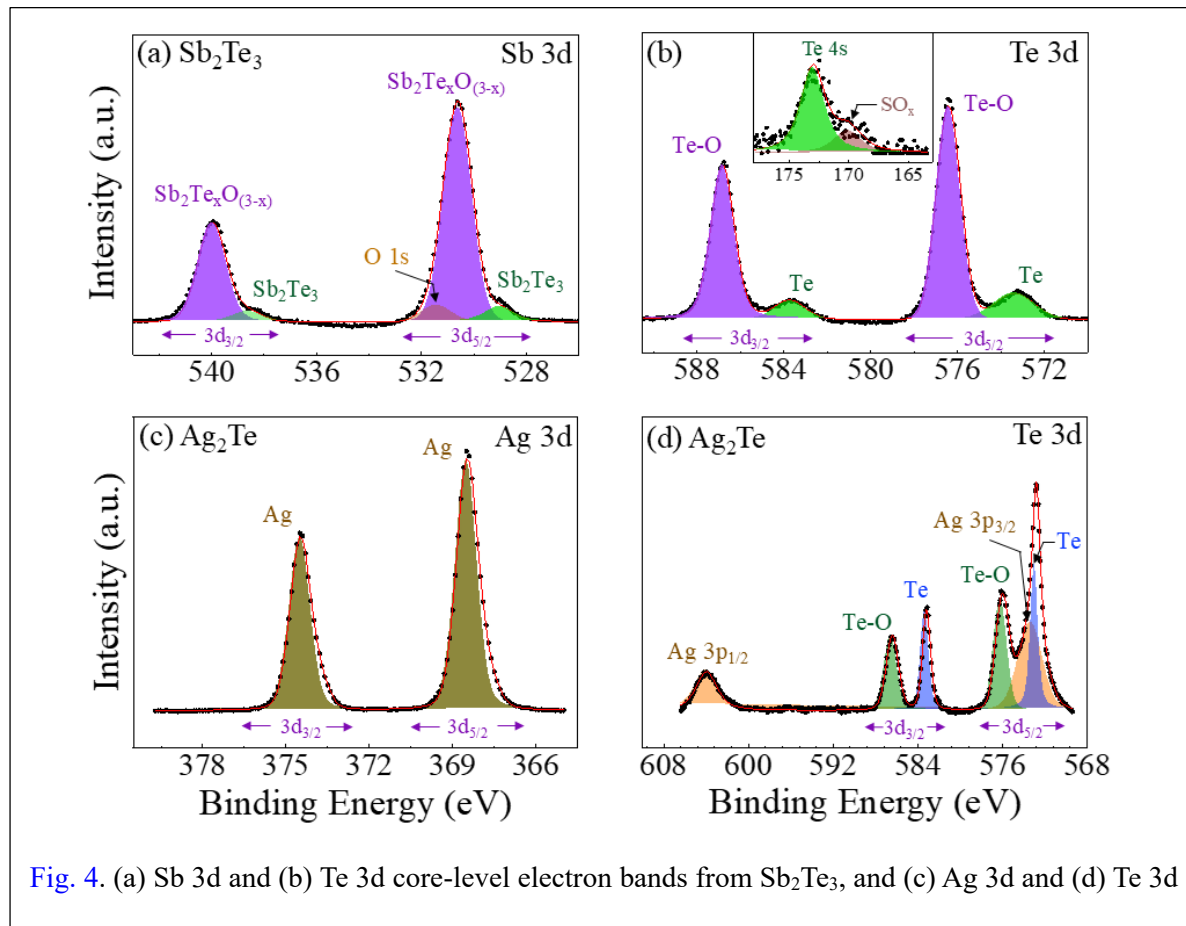
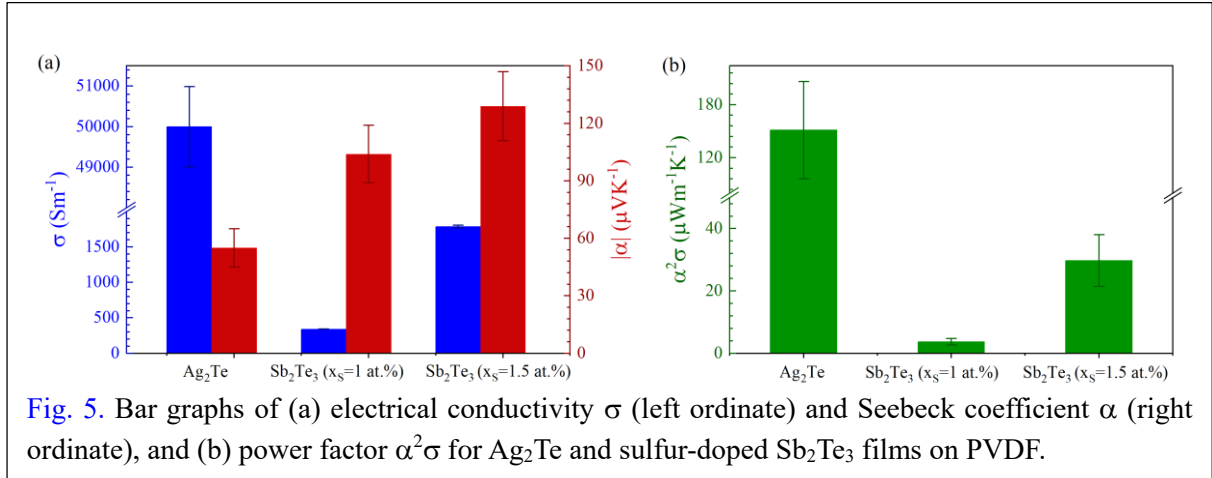


Fig. 4. (a) Sb 3d and (b) Te 3d core-level electron bands from Sb₂Te₃, and (c) Ag 3d and (d) Te 3d

3.4. Thermoelectric properties of films of Ag₂Te and Sb₂Te₃ nanostructure assemblies on PVDF

Figs. 5a-b summarizes the electrical conductivity σ measured and Seebeck coefficient α determined from Ag₂Te and Sb₂Te₃ films. Ag₂Te films show the highest $\sigma = 50000 \pm 990 \text{ Sm}^{-1}$ and a power factor $\alpha^2\sigma = 150 \pm 55.1 \mu\text{Wm}^{-1}\text{K}^{-1}$ and $\alpha = -55 \pm 10 \mu\text{VK}^{-1}$ indicating n-type conduction. Sb₂Te₃ films with both sulfur doping levels $x_S=1$ at.% and 1.5 at.% show $\alpha>0$, indicating p-type behavior. Higher sulfur doping results in a fivefold higher $\sigma = 1800 \pm 3.4 \text{ Sm}^{-1}$, a ~25% higher $\alpha \sim 130 \pm 18 \mu\text{VK}^{-1}$, and an eightfold higher power factor $\alpha^2\sigma = 30 \pm 8.3 \mu\text{Wm}^{-1}\text{K}^{-1}$. These enhancements correlate with twenty-fold higher hole concentration $h = 8.80 \times 10^{19} \text{ cm}^{-3}$ for $x_S=1.5$ at.% than $h = 4.30 \times 10^{18} \text{ cm}^{-3}$ for $x_S = 1$ at.%

indicated by room-temperature Hall measurements (Table S2). Thus, the sulfur doping level is a key factor to tailor electronic transport and thermoelectricity in Sb_2Te_3 , consistent with prior works¹⁶.



3.5. Thermoelectric device fabrication and power generation characteristics

A six-leg p-n junction thermoelectric device is fabricated by integrating alternating PVDF strips with Ag_2Te and 1.5 at.% sulfur-doped Sb_2Te_3 films onto a polyimide substrate (Fig. 6a). Mechanical bending significantly increases the device electrical resistance (see Fig. 6b) linearly with apex bending angle for $0^\circ < \theta < \sim 50^\circ$. At higher angles (e.g., $\theta \sim 60^\circ$) the resistance increases at a lower rate, yielding a cumulative resistance increase of $\sim 12.5\%$ at the highest angle $\theta \sim 99.7^\circ$. No discernible macroscale changes in the film are revealed by SEM images, suggesting that the bending-induced resistance changes likely arise from small perturbations in between nanostructures relative to each other, the PVDF membrane and the metal contacts.

Repeated bending with $\theta_{\text{min}} = 0^\circ$ and $\theta_{\text{max}} \sim 80^\circ$ shows a monotonic increase in resistance with increasing number of bending cycles n_{bending} (Fig. S10). The $\sim 124\%$ increase in resistance for $n_{\text{bending}} = 200$ cycles is larger than that reported for Zn-doped Sb_2Te_3 films deposited Sb/Zn magnetron sputtering and Te evaporation followed by annealing⁵⁰. This large change is attributable to inter-nanostructure microcracking in the films (see inset in Fig. S10) that disrupt low-conductance network paths^{22, 51}. Including a low-resistance binder⁵² could potentially counter this behavior.

Our six-leg devices show an output voltage $V_{OC} = 33.6$ mV for $\Delta T = 50$ °C, and a maximum power output $P_{OC} = 120$ nW at $\Delta T = 30$ °C (Figs. 6c-d). The estimated voltage and power outputs per gram,

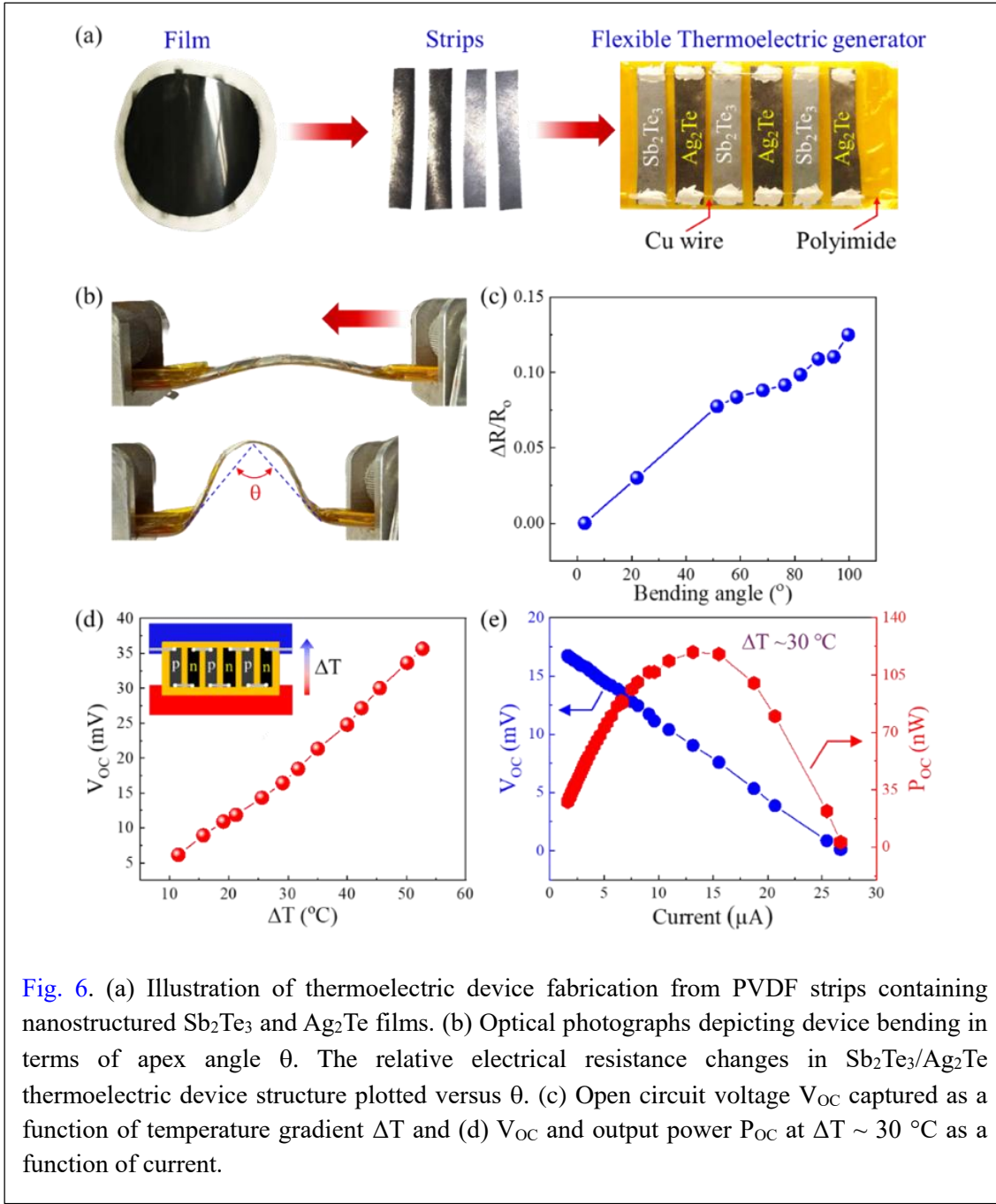


Fig. 6. (a) Illustration of thermoelectric device fabrication from PVDF strips containing nanostructured Sb_2Te_3 and Ag_2Te films. (b) Optical photographs depicting device bending in terms of apex angle θ . The relative electrical resistance changes in Sb_2Te_3/Ag_2Te thermoelectric device structure plotted versus θ . (c) Open circuit voltage V_{OC} captured as a function of temperature gradient ΔT and (d) V_{OC} and output power P_{OC} at $\Delta T \sim 30$ °C as a function of current.

namely, are $V_m \sim 396$ mV/g for $\Delta T \sim 50$ °C and $P_m \sim 1.24$ μ W/g for $\Delta T \sim 30$ °C (Table S3) surpass reported values for Sb_2Te_3 /membrane and paper-based devices^{35,36}, but are inferior to the state-of-the-art thermoelectric devices (see supplementary Table S4). A human finger touch produced ~ 2.6 mV from our thermoelectric device (See supplementary movie S1). These findings demonstrate that films from microwave-synthesized nanostructures on PVDF are promising as heat-harvesting power generators. The relatively high internal resistance of ~ 850 Ω in our devices are likely due to surface oxidation and

organic capping of the nanostructures, which could be addressed through post-deposition surface oxide reduction by hydrazine, acid treatments to remove organics^{40, 52}, and thermal annealing.

4. Conclusions

Ag-rich Ag₂Te nanowires and sulfur-doped Sb₂Te₃ nanoplates were produced by rapid microwave synthesis, yielding gram-scale quantities of high-quality materials within minutes. Sulfur doping in the 1~1.5 at.% range in Sb₂Te₃ leads to an eightfold power factor increase driven by a fivefold improvement in electrical conductivity and a ~1.25-fold increase in the Seebeck coefficient. Six-leg p-n junction devices fabricated from nanostructured films of Ag₂Te and sulfur-doped Sb₂Te₃ on PVDF exhibit promising characteristics such as a maximum voltage of ~33.6 mV for $\Delta T = 50$ °C and a maximum power of ~120 nW at $\Delta T = 30$ °C. These results highlight the promise of rapid synthesis of high-quality nanomaterials and their utility for thermoelectric power generation for flexible electronics devices. Process optimization and engineering inter-nanostructure interactions during bending should pave way for efficient, lightweight, and sustainable energy harvesting technologies.

Conflicts of interest: There are no conflicts to declare.

Data availability

The data supporting this article have been included as part of the supplementary information (SI). Supplementary information is available.

Acknowledgements

A.S. and A.K. acknowledge research facility at IIT Mandi and funding from Department of Science and Technology, New Delhi, India. P. E. acknowledges funding from the Knut and Alice Wallenberg Foundation through the Wallenberg Academy Fellows program (grant no. KAW 2020.0196, and the Swedish Research Council under project grants no 2021-03826, and 2025-03680. G.R. acknowledges funding support from the US National Science Foundation grant CMMI 2135725 through the BRITE program, the Empire State Development's Division of Science, Technology and Innovation Focus Center at RPI, C210117, Wallenberg Initiative in Materials Science for Sustainability (WISE) funded by the Knut and Alice Wallenberg Foundation, and a Swedish Research Council grant under VR project 2024-04996.

References

1. B. Lee, H. Cho, K. T. Park, J.-S. Kim, M. Park, H. Kim, Y. Hong and S. Chung, *Nature Communications*, 2020, **11**, 5948.
2. M. Sattar, Y. J. Lee, H. Kim, M. Adams, M. Guess, J. Kim, I. Soltis, T. Kang, H. Kim, J. Lee, H. Kim, S. Yee and W.-H. Yeo, *ACS Applied Materials & Interfaces*, 2024, **16**, 37401-37417.
3. X. He, X.-L. Shi, X. Wu, C. Li, W.-D. Liu, H. Zhang, X. Yu, L. Wang, X. Qin and Z.-G. Chen, *Nature Communications*, 2025, **16**, 2523.
4. C. Xu, Y. Song, M. Han and H. Zhang, *Microsystems & Nanoengineering*, 2021, **7**, 25.
5. J. Yuan and R. Zhu, *Applied Energy*, 2020, **271**, 115250.
6. A. Rahmanudin, Z. Khan, K. Tybrandt and N. Kim, *Journal of Materials Chemistry A*, 2023, **11**, 22718-22736.
7. D. M. Rowe, *Thermoelectrics handbook: macro to nano*, CRC press, 2018.
8. T. Cardinal, M. Kwan, T. Borca-Tasciuc and G. Ramanath, *Applied Physics Letters*, 2016, **109**.
9. T. Cardinal, M. Kwan, T. Borca-Tasciuc and G. Ramanath, *ACS Applied Materials & Interfaces*, 2017, **9**, 2001-2005.
10. T. Cardinal, Devender, T. Borca-Tasciuc and G. Ramanath, *ACS Applied Materials & Interfaces*, 2016, **8**, 4275-4279.
11. Devender, R. J. Mehta, K. Lofgreen, R. Mahajan, M. Yamaguchi, T. Borca-Tasciuc and G. Ramanath, *Journal of Vacuum Science & Technology A*, 2015, **33**, 020605.
12. Devender, K. Lofgreen, S. Devasenathipathy, J. Swan, R. Mahajan, T. Borca-Tasciuc and G. Ramanath, *Journal of Vacuum Science & Technology A*, 2015, **33**, 060611.
13. Y. Du, J. Xu, B. Paul and P. Eklund, *Applied Materials Today*, 2018, **12**, 366-388.
14. Q. Yang, S. Yang, P. Qiu, L. Peng, T.-R. Wei, Z. Zhang, X. Shi and L. Chen, *Science*, 2022, **377**, 854-858.
15. R. J. Mehta, Y. Zhang, C. Karthik, B. Singh, R. W. Siegel, T. Borca-Tasciuc and G. Ramanath, *Nature Materials*, 2012, **11**, 233-240.
16. R. J. Mehta, Y. Zhang, H. Zhu, D. S. Parker, M. Belley, D. J. Singh, R. Ramprasad, T. Borca-Tasciuc and G. Ramanath, *Nano Letters*, 2012, **12**, 4523-4529.
17. A. Soni, Z. Yanyuan, Y. Ligen, M. K. K. Aik, M. S. Dresselhaus and Q. Xiong, *Nano Letters*, 2012, **12**, 1203-1209.
18. P. Jood, R. J. Mehta, Y. Zhang, G. Peleckis, X. Wang, R. W. Siegel, T. Borca-Tasciuc, S. X. Dou and G. Ramanath, *Nano Letters*, 2011, **11**, 4337-4342.
19. Y. Ding, Y. Qiu, K. Cai, Q. Yao, S. Chen, L. Chen and J. He, *Nature Communications*, 2019, **10**, 841.
20. A. Kashyap, D. Rawat, D. Sarkar, N. K. Singh, K. Biswas and A. Soni, *Angewandte Chemie International Edition*, 2024, **63**, e202401234.

21. A. K. Gautam, H. H. Singh and N. Khare, *Nano Energy*, 2023, **107**, 108125.
22. A. Soni, Y. Shen, M. Yin, Y. Zhao, L. Yu, X. Hu, Z. Dong, K. A. Khor, M. S. Dresselhaus and Q. Xiong, *Nano Letters*, 2012, **12**, 4305-4310.
23. B. Paul, J. Lu and P. Eklund, *ACS Applied Materials & Interfaces*, 2017, **9**, 25308-25316.
24. Y. Deng, M. Wei, Y. Lei, J. Lu, P. Peng, Y. Zhang and Z. Zheng, *CrystEngComm*, 2025.
25. L. D. Hicks and M. S. Dresselhaus, *Physical Review B*, 1993, **47**, 12727-12731.
26. M. Tan, L. Hao, H. Li, C. Li, X. Liu, D. Yan, T. Yang and Y. Deng, *Scientific Reports*, 2020, **10**, 5978.
27. C. Wu, Y. Liu, J. Li, M. Zhang, Z. Wang and K. Cai, *ACS Applied Materials & Interfaces*, 2024, **16**, 39623-39630.
28. J. Du, B. Zhang, M. Jiang, Q. Zhang, K. Zhang, Y. Liu, L. Wang and W. Jiang, *Advanced Functional Materials*, 2023, **33**, 2213564.
29. P. Wanarattikan, P. Jitthammapirom, R. Sakdanuphab and A. Sakulkalavek, *Advances in Materials Science and Engineering*, 2019, **2019**, 6954918.
30. M. Wei, H. Li, M. Nisar, Z. Zhang, F. Li, G. Liang, J. Luo, Z. Zheng, Y. Chen and Z. Zheng, *Chemical Engineering Journal*, 2024, **495**, 153185.
31. J. Gao, L. Miao, C. Liu, X. Wang, Y. Peng, X. Wei, J. Zhou, Y. Chen, R. Hashimoto, T. Asaka and K. Koumoto, *Journal of Materials Chemistry A*, 2017, **5**, 24740-24748.
32. L. M. Goncalves, P. Alpuim, A. G. Rolo and J. H. Correia, *Thin Solid Films*, 2011, **519**, 4152-4157.
33. S. A. Haidar, Y. Gao, Y. He, J. E. Cornett, B. Chen, N. J. Coburn, C. Glynn, M. T. Dunham, K. E. Goodson and N. Sun, *Thin Solid Films*, 2021, **717**, 138444.
34. D. W. Newbrook, S. P. Richards, V. K. Greenacre, A. L. Hector, W. Levason, G. Reid, C. H. K. de Groot and R. Huang, *ACS Applied Energy Materials*, 2020, **3**, 5840-5846.
35. Z. Dong, H. Liu, X. Yang, J. Fan, H. Bi, C. Wang, Y. Zhang, C. Luo, X. Chen and X. Wu, *npj Flexible Electronics*, 2021, **5**, 6.
36. X. Zhao, W. Han, C. Zhao, S. Wang, F. Kong, X. Ji, Z. Li and X. Shen, *ACS Applied Materials & Interfaces*, 2019, **11**, 10301-10309.
37. T. Varghese, C. Hollar, J. Richardson, N. Kempf, C. Han, P. Gamarachchi, D. Estrada, R. J. Mehta and Y. Zhang, *Scientific Reports*, 2016, **6**, 33135.
38. Y. Xu, B. Wu, C. Hou, Y. Li, H. Wang and Q. Zhang, *Global Challenges*, 2024, **8**, 2300032.
39. J. Andzane, E. Spalva, J. Katkevics, L. Bugovecka, A. Kons, K. Buks and D. Erts, *ACS Applied Energy Materials*, 2023, **6**, 10807-10816.
40. R. J. Mehta, C. Karthik, B. Singh, R. Teki, T. Borca-Tasciuc and G. Ramanath, *ACS Nano*, 2010, **4**, 5055-5060.

41. F. Xiao, G. Chen, Q. Wang, L. Wang, J. Pei and N. Zhou, *Journal of Solid State Chemistry*, 2010, **183**, 2382-2388.
42. Y. Chang, J. Guo, Y.-Q. Tang, Y.-X. Zhang, J. Feng and Z.-H. Ge, *CrystEngComm*, 2019, **21**, 1718-1727.
43. H. J. Im, B. Koo, M.-S. Kim and J. E. Lee, *Applied Surface Science*, 2019, **475**, 510-514.
44. H. Yang, J.-H. Bahk, T. Day, A. M. S. Mohammed, B. Min, G. J. Snyder, A. Shakouri and Y. Wu, *Nano Letters*, 2014, **14**, 5398-5404.
45. D. Pinisetty, M. Gupta, A. B. Karki, D. P. Young and R. V. Devireddy, *Journal of Materials Chemistry*, 2011, **21**, 4098-4107.
46. M. C. Biesinger, *Applied Surface Science*, 2022, **597**, 153681.
47. B. Xin, A. Le Febvrier, L. Wang, N. Solin, B. Paul and P. Eklund, *Materials & Design*, 2021, **210**, 110033.
48. J. Pei, G. Chen, D. Jia, Y. Yu, J. Sun, H. Xu and Z. Qiu, *New Journal of Chemistry*, 2014, **38**, 59-62.
49. T. Wang, R. Mehta, C. Karthik, P. G. Ganesan, B. Singh, W. Jiang, N. Ravishankar, T. Borca-Tasciuc and G. Ramanath, *The Journal of Physical Chemistry C*, 2010, **114**, 1796-1799.
50. Z.-l. Zhang, W.-y. Yang, B. Wu, M. Nisar, F. Li, G.-x. Liang, J.-t. Luo, Y.-x. Chen and Z.-h. Zheng, *Chemical Science*, 2025, **16**, 3638-3645.
51. G. Okram, A. Soni and R. Rawat, *Nanotechnology*, 2008, **19**, 185711.
52. B. Zhang, J. Sun, H. E. Katz, F. Fang and R. L. Opila, *ACS Applied Materials & Interfaces*, 2010, **2**, 3170-3178.

Supporting Information for
Morphology-engineered nanostructured silver- and antimony-telluride films for flexible thermoelectric generators

Ankit Kashyap^{a,b}, Conner Wallace^b, Geetu Sharma^b, Collin Rowe^b, Mahima Sasikumar^b, Niraj Kumar Singh^d, Per Eklund^{d,e}, Theodorian Borca-Tasciuc^c, Ganpati Ramanath^{b,d,e*}, and Ajay Soni^{a*}

^a*School of Physical Sciences, Indian Institute of Technology Mandi, 175005, Himachal Pradesh, India.*

^b*Rensselaer Polytechnic Institute, Materials Science & Engineering Department, Troy, NY 12180, USA.*

^c*Rensselaer Polytechnic Institute, Department of Mechanical Engineering, Troy, NY 12180, USA.*

^d*Inorganic Chemistry, Ångström Laboratory, Uppsala University, SE-751 21 Uppsala, Sweden.*

^e*Wallenberg Initiative Materials Science for Sustainability (WISE), Uppsala University, Sweden.*

*Corresponding authors: ganapr@rpi.edu, ganpati.ramanath@kemi.uu.se and ajay@iitmandi.ac.in

The data and explanations provided below supplement the narrative and figures in the main manuscript.

1. Custom-built setup used for flexible thermoelectric device measurements

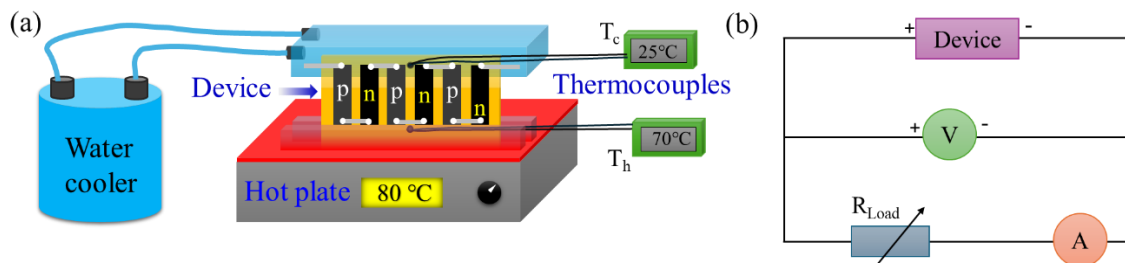


Figure S1. Schematic of the (a) custom setup used for the measurement and (b) circuit diagram of measurement.

Performance evaluation of flexible thermoelectric generators is done using a custom-built performance measurement system. Lateral temperature gradient is applied using a hot plate and a water-cooled aluminium block on the hot and cold side respectively. The temperature on cold and hot side was measured by attaching a E-type thermocouple of diameter (100 μ m) on the device. Output voltage as a function of ΔT is measured using Keithley multimeter 2000 and for the output power measurement variable resistance is connected in series to the source meter as shown in the circuit diagram **Figure S1**. The power output measurement of flexible thermoelectric generator was measured using Keithley source meter 2400 (measure the current output) and Keithley multimeter 2000 (measure the output voltage) through a LabVIEW program.

2. Lattice parameters from x-ray diffraction

Material	a (Å)	b (Å)	c (Å)	Lattice volume (Å ³)
----------	-------	-------	-------	----------------------------------

Sb_2Te_3	4.2720	4.2720	30.3953	480.4013
Ag_2Te	8.1671	4.4697	8.9795	271.1747

Table S1. Lattice parameters obtained using Rietveld refinement of Sb_2Te_3 and Ag_2Te .

Lattice parameters of Sb_2Te_3 and Ag_2Te were extracted through Rietveld refinement of the powder X-ray diffraction data. Refinements were performed using *FullProf* software employing a pseudo-Voigt profile function and polynomial background fitting. The refined lattice parameters, lattice volumes, are summarized in [Table S1](#).

3. Size distribution of Sb_2Te_3 nanoplates and Ag_2Te nanowires

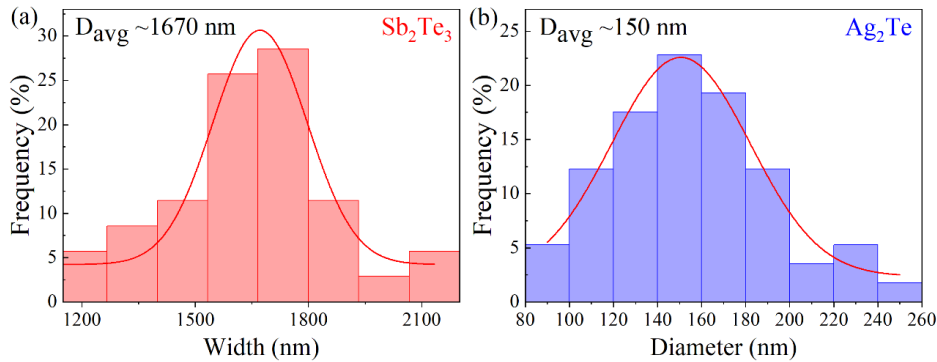


Figure S2. Size distribution of microwave synthesized (a) Sb_2Te_3 nanoplates and (b) Ag_2Te nanowires.

Size distribution of microwave synthesized Sb_2Te_3 nanoplates and Ag_2Te nanowires was measured from scanning electron microscopy (SEM) images using ImageJ software. The average size of Sb_2Te_3 nanoplatelets and diameter of Ag_2Te nanowires obtained from SEM images are ~ 1670 nm \pm 208 nm and ~ 150 nm \pm 37 nm, respectively.

4. Elemental distributions in nanostructures

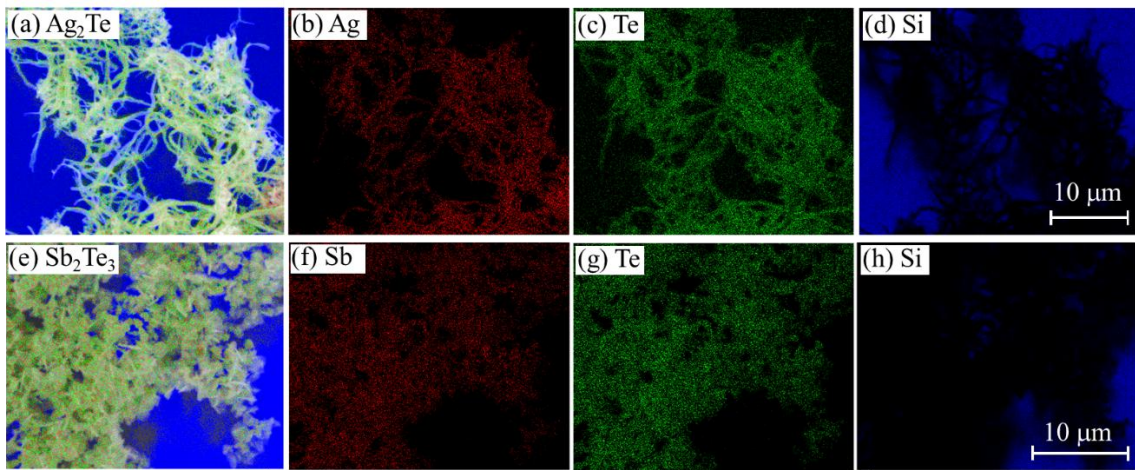


Figure S3. Elemental mapping of Ag_2Te nanowires: (a) combined elemental map, (b) Ag distribution, (c) Te distribution, and (d) Si distribution. Elemental mapping of Sb_2Te_3 nanoplates: (e) combined map, (f) Sb distribution, (g) Te distribution, and (h) Si distribution.

A field-emission Zeiss Supra 55 SEM equipped with an energy dispersive X-ray (EDX) detector was used to collect elemental maps and to examine the morphology of the nanostructures. All EDX measurements were performed at an accelerating voltage of 20 keV.

5. Ag_2Te nanowires formation dependence of reaction conditions

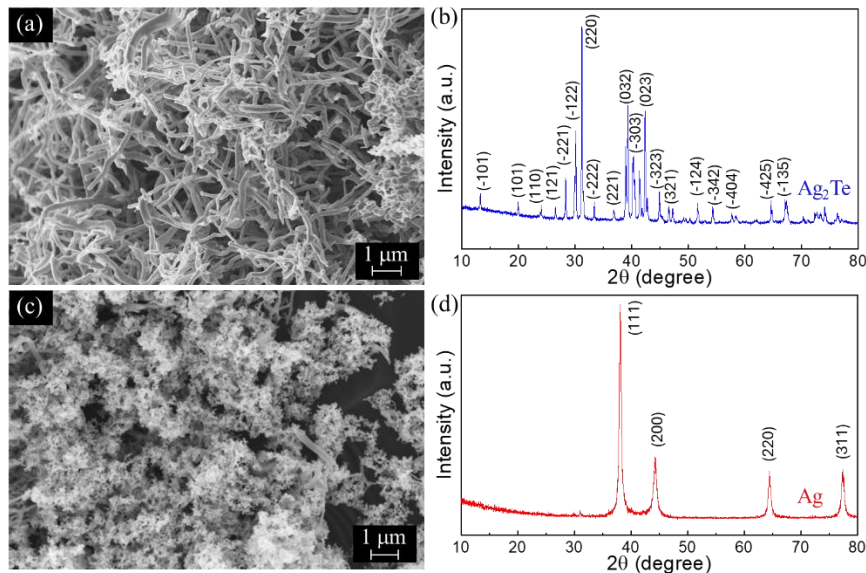


Figure S4. Scanning electron micrographs of (a) pulsed microwave heated reaction, (b) x-ray diffraction patterns of Ag_2Te (c) Ag nanoparticles and (d) x-ray diffraction patterns of Ag.

The formation of Ag_2Te nanowires was found to depend strongly on the microwave-heating conditions. Cyclic microwave heating, where the power is periodically switched on and off, promotes the growth of Ag_2Te nanowires. In contrast, continuous (non-cycled) microwave heating results in the formation of Ag nanoparticles instead, as shown in [Figure S4](#).

6. X ray diffraction patterns of Sb_2Te_3 synthesized using TOP and TOPO

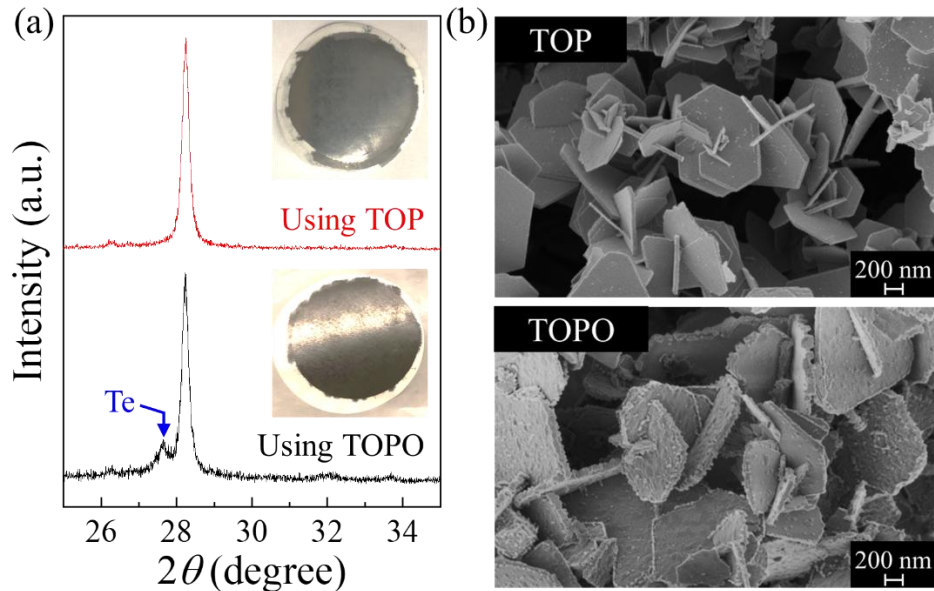


Figure S5. (a) X-ray diffraction patterns of Sb_2Te_3 synthesized using TOP (red) and TOPO (blue), highlighting structural differences, with inset images showcasing the corresponding films. (b) Scanning electron microscopy images showing Sb_2Te_3 synthesized using TOP with smooth hexagon, and TOPO with rough hexagonal morphology.

7. Effect of precursor amounts on Sb_2Te_3 morphology

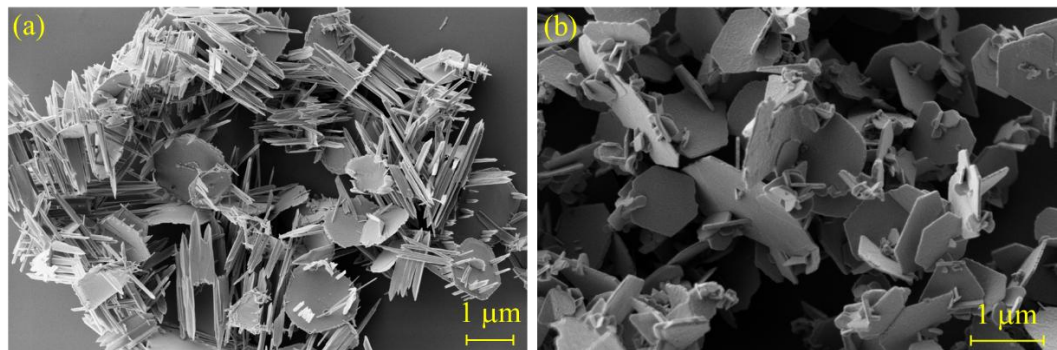


Figure S6. SEM images showing the effect of precursor amounts on Sb_2Te_3 morphology.

(a) Heterostructure hexagons with rod-like edges formed at low precursor amounts (0.04 mmol SbCl_3 in 6.25 ml 1,5-pentanediol, 0.08 mmol Te in 2 ml TOP). (b) No rods observed at higher amounts (0.15 mmol SbCl_3 and 0.30 mmol Te).

8. Cross-section SEM images of Ag_2Te and Sb_2Te_3 films

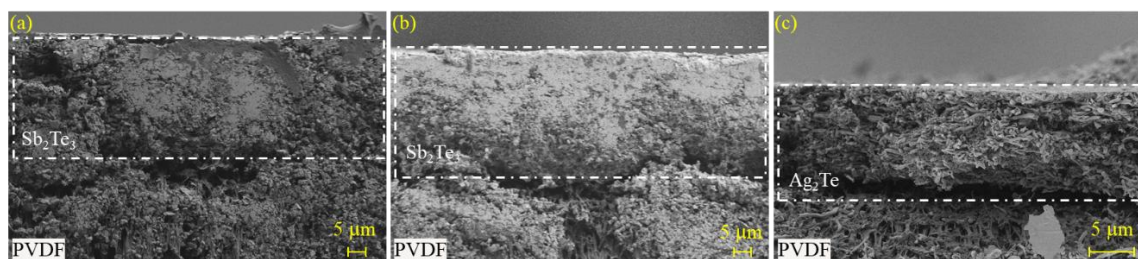


Figure S7. Cross-section SEM images of flexible films of (a) Sb_2Te_3 ($x_{\text{S}} = 1.5$ at.%)1 (b) Sb_2Te_3 ($x_{\text{S}} = 1$ at.%) and (c) Ag_2Te .

Cross-sectional measurements were performed on freshly fractured films using a Zeiss Supra 55 field-emission SEM. Obtained micrographs were used to estimate the thickness of films.

9. X-ray photoelectron spectroscopy Ag_2Te and Sb_2Te_3 films

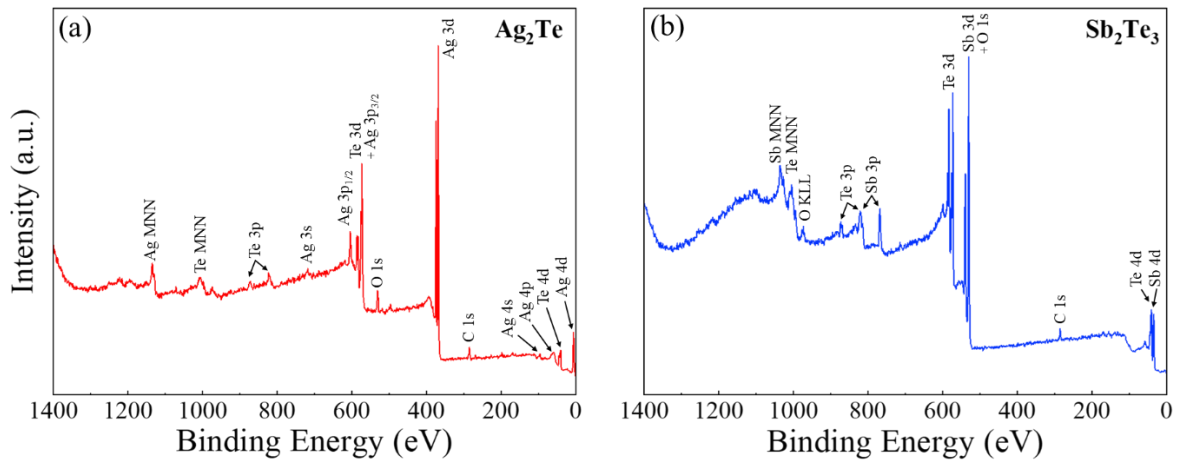


Figure S8. X-ray photoelectron spectroscopy survey scan of (a) Ag_2Te and (b) Sb_2Te_3 film.

X-ray photoelectron spectroscopy (XPS) measurements in a PHI 5000 Versaprobe system were used to characterize the surface chemistry of Ag_2Te and Sb_2Te_3 films. Al $\text{K}\alpha$ X-rays were used as a source on 100 μm spot size. XPS analyses were performed using MultiPak software (ULVAC-PHI, Inc.) to subtract background by the Shirley method, and corrected charging-related energy shifts with reference to the adventitious carbon peak.

10. X-ray photoelectron spectroscopy of Sb_2Te_3 films

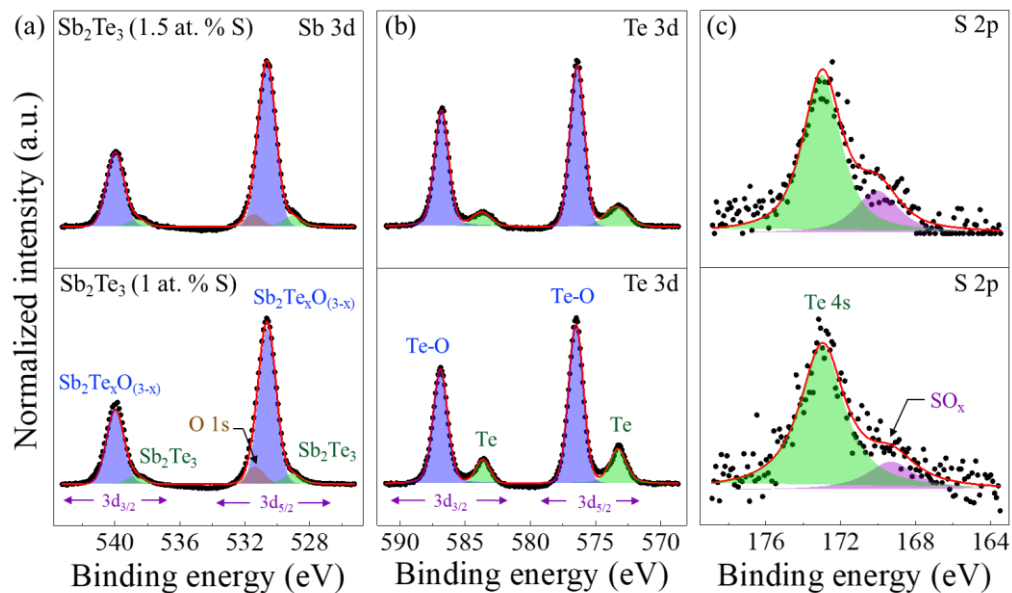


Figure S9. Comparison of x-ray photoelectron spectroscopy survey scan of (a) Sb 3d, (b) Te 3d and (c) S 2p for oxidised Sb_2Te_3 film with 1.5 at. % sulfur and 1 at. % sulfur.

11. Relative electrical resistance change with bending cycles

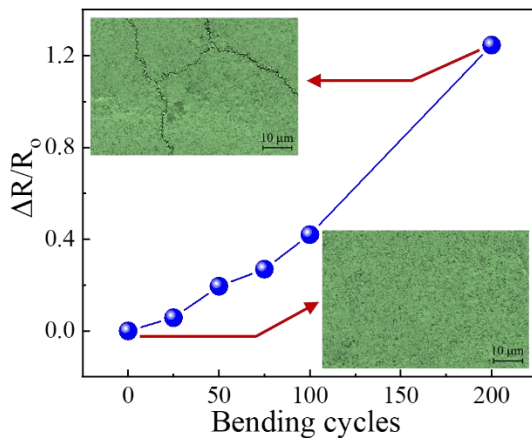


Figure S10. The relative electrical resistance changes with the number of bending cycles for bending between $\theta_{\min}=0^\circ$ and $\theta_{\max}\sim 80^\circ$ (inset showing SEM micrographs with highlighted crack area)

The electrical resistance as a function the bending cycle change was performed using a an Instron 5843 system by connecting ends of the flexible thermoelectric generator to a Keithley 2000 multimeter. SEM micrographs of the Sb_2Te_3 film on the flexible thermoelectric generator taken before and after bending the device films with the crack regions clearly highlighted and color-enhanced to improve visibility.

12. Hall measurement data of Ag_2Te and Sb_2Te_3 films

Sample	n (cm^{-3})	μ ($\text{cm}^2\text{V}^{-1}\text{s}^{-1}$)
Sb_2Te_3 ($x_{\text{S}} = 1$ at.%)	4.30E+18	4.95E+00
Sb_2Te_3 ($x_{\text{S}} = 1.5$ at.%)	8.80E+19	1.27E+00
Ag_2Te	4.21E+21	7.42E-01

Table S2. Hall measurement data of Sb_2Te_3 and Ag_2Te films.

Hall measurements in an apparatus with a ~ 0.485 T permanent magnet. Hall voltages were measured in van der Pauw geometry using a Keithley 2100 multimeter for a 10 mA current delivered by a Keithley 2400 source.

13. Estimated output voltage and output power per gram

Device	Voltage output per gram (50 K)	Power output per gram (30 K)
$\text{Sb}_2\text{Te}_3/\text{Ag}_2\text{Te}$ (6 leg device)	~ 396 mV/g	1.24 $\mu\text{W/g}$

Table S3. Estimated voltage output and power output per gram at temperature difference of 50 K and 30 K respectively.

Voltage and power output per gram were calculated based on the measured device voltage and power output, normalized by the total mass of active material used in fabricating the device.

14. Comparison of flexible device performance with the literature

Material	Number of legs	Power (nW)	ΔT (K)	Ref.
Sb ₂ Te ₃ /Ag ₂ Te	6	~120	~30	This work
Sb ₂ Te ₃ /Bi ₂ Te ₃	6	~ 0.35	~30	¹
Bi _{0.5} Sb _{1.5} Te ₃ /Bi ₂ Se _{0.3} Te _{2.7}	10	10	~35	²
Bi ₂ Te _{2.8} Se _{0.2}	5	1400	~30	³
Sb ₂ Te ₃ /MXene	7	2000	~30	⁴

Table S4. Comparison of device performance with prior relevant reports.

References

1. Z. Dong, H. Liu, X. Yang, J. Fan, H. Bi, C. Wang, Y. Zhang, C. Luo, X. Chen and X. Wu, *npj Flexible Electronics*, 2021, **5**, 6.
2. X. Zhao, W. Han, C. Zhao, S. Wang, F. Kong, X. Ji, Z. Li and X. Shen, *ACS Applied Materials & Interfaces*, 2019, **11**, 10301-10309.
3. T. Varghese, C. Hollar, J. Richardson, N. Kempf, C. Han, P. Gamarachchi, D. Estrada, R. J. Mehta and Y. Zhang, *Scientific Reports*, 2016, **6**, 33135.
4. Y. Xu, B. Wu, C. Hou, Y. Li, H. Wang and Q. Zhang, *Global Challenges*, 2024, **8**, 2300032.